Supplementary Information

Boosting oxygen evolution stability and activity of hierarchical IrRu bimetallic coating on WO_3 nano-arrays electrode for PEM water electrolysis

Guang Jiang [a,b], Hongmei Yu [a*], Dewei Yao [a,b], Yonghuan Li [a,b], Jun Chi [a], Hongjie Zhang [a], Zhigang Shao [a*]

[a] Fuel Cell System and Engineering Laboratory, Key Laboratory of Fuel Cells & Hybrid Power Sources, Dalian Institute of Chemical Physics, Chinese Academy of Sciences, Dalian 116023, China

[b] University of Chinese Academy of Sciences, Beijing, 100049, China

Corresponding Author *
E-mail: hmyu@dicp.ac.cn, zhgshao@dicp.ac.cn.

Experimental

Materials

$SC(NH_2)_2$, $C_4H_4O_4$, CH_3CN, $H_2C_2O_4$ are purchased from Kermel (Tianjin, China). Electrolyte membranes are purchased from Fumatech (120 μm) and DuPont (Nafion® 115, 125μm). Nafion ionomer solution (5 wt%) is also purchased from DuPont. Pt/C(70 wt%) and Ir Black are purchased from Johnson Matthey. H_2IrCl_6 and $RuCl_3$ are purchased from Borui Co., Ltd, KunMing.

Preparation of IrRu@WO_3 electrode

WO_3 nanonorod is synthesized by hydrothermal method and supported on W foil at 180 °C for 6 h based on our previous work [1]. As Fig. 1a diagramed, Ru spices is electrodeposited on WO_3 nanorod surface firstly. In specific, WO_3 nanorod loading on the W foil (2.5*2.5 cm^2) is immersed into $RuCl_3$ solution (5.0 g/L, oxalate: 3.5 g/L) and conducted electrodepositing under -10 mA cm^{-2} at 80 °C. Then, second electrodepositing for Ir component is carried out by immersing the intermediate Ru@WO_3 foil in H_2IrCl_6 solution (10.0 g/L, oxalate: 3.5 g/L) by cyclic voltammetry (-0.4~0.05 V) at 80 °C. Finally, obtained IrRu@WO_3 electrode is annealed in Ar atmosphere for 2 h.

Physical & Electrochemical Characterizations

Scanning electron microscope (SEM, FE-7800), transmission electron microscope (TEM, JEOL-2000EX) and spherical aberration corrected transmission electron microscope (ac-TEM, JEM-ARM200F) coupled EDX are conducted to define the morphologies. Crystal structure and valence are analyzed by glancing angle x-ray diffraction (GIXRD, Empyrean-100) and X-ray photoelectron spectroscopy (XPS, Thermo Escalab 250Xi). Noble metal content is examined by inductively coupled plasma mass spectrometry (ICP-OES, 7300DV). OER performance is investigated in 0.5 M H_2SO_4 at 30 °C supported by a counter and reference electrode of graphite plate and saturated calomel electrode (SCE). Cyclic voltammetry (CV, scan rate: 50 mV s^{-1}) and linear scan voltammetry (LSV, scan rate: 5 mV s^{-1}) are executed. According to eq 1) and 2) [2], voltammetric charge Q and ECSA can be estimated and based on the active integral area from CV curves and ECSA-charge constant of 1681 cm^2 C^{-1}. OER stability based on half-cell is evaluated by serial chronoamperometries (10, 30, 50, 100 mA cm^{-2}). As metallic Ir and Ru serve OER activity site, the charge Q of CV can illustrate the actual valence change from metal to oxide catalyst and, which implies the electron transfer on the electrode surface. TOF is electron turnover frequency for per electrochemical surface site that means the current for per surface voltammetry charge Q. Therefore, TOF can be calculated as eq3. An online gas spectrometry (GC) is coupled to a single cell test station to analyze the produced oxygen. After passing through a silica gel column to remove the vapor, anode gas volume flow is recorded by gas flow counter and GC to record the dry oxygen flow and purity. Faradic efficiency can be calculated by the following eq4-6.

$$Q = {}^{S}/_{\upsilon} \quad \text{Eq. S1)}$$

$$ECSA = {}^{Q \times C}/_{M} \quad \text{Eq. S2)}$$

$$TOF = \frac{I}{4Fn} = \frac{I}{Q} \quad \text{Eq. S3)}$$

$$FE = \frac{4 \cdot F \cdot n_{O2}}{I} \quad \text{Eq. S4)}$$

$$n_{O_2} = \frac{p}{RT} \cdot V_{O_2} \quad \text{Eq. S5)}$$

$$V_{O_2} = V \cdot x_{O_2} \quad \text{Eq. S6)}$$

Where: S is the integral area in CV curve (A·V); C is the ECSA-charge constant of 1681 cm_{ecs}^2 C^{-1}; υ is the scanning rate (V s^{-1}); M is the geometric area Ir loading (mg cm^{-2}). I is the current density, A cm^{-2}, Q is the voltammetry charge of during the cyclic voltammetry scan, C cm^{-2}, F is Faraday constant (96 485.3 C·mol^{-1}), n_{O2} is the molar flow of oxygen per electrode area, mol s^{-1} cm^{-2}. The 4 is a factor that derives from the fact that four electrons have to be transferred during the reaction to form one oxygen molecule. I is the current density, A cm^{-2}. p or T is the pressure (1.01*10^6 pa) or temperature (T, 293.1) of the surrounding. V_{O_2} is volume flow of oxygen, m^3 s^{-1}. The V is average volume flow of dried anode gas per electrode area, m^3 s^{-1} cm^{-2}. x_{O_2} is the O_2 concentration detected by (GC).

The terminal IrRu@WO_3 electrode loaded on W foil, which serves anode, is decaled to the blank side of a Pt/C spraying membrane and hot-pressed at a condition of 2 MPa and 140 °C for 3 min. Especially, electrolyte membrane is beforehand modified by sprayed Nafion layer (0.2 mg cm^{-2}) on both sides.[3] Pt/C ink is sprayed on cathode side with Pt loading of 0.4 mg cm^{-2}. Then, membrane electrode assemblies (MEA) is hot-pressed by placing a wet-proof carbon paper on cathode side at 0.1 MPa, 140 °C for 2 min (active area: 2.0*2.0 cm^2). MEA is tested by a pair of home-made Ti end plates with torque of 5.0 N m. Pt-coated porous Ti (0.8 mm in thickness) serves anode gas diffusion layer. Water is pumped to anode cavity and heated to 80 °C by heating rod penetrated in end plates. *I-V* curve is recorded via controlling the current density with step sizes of 50 and 100 mA cm^{-2} per 30 s in the ranges of 0~1.0 and 1.0~2.0 A cm^{-2}, respectively. Electrochemical impedance spectroscopy (*EIS)* is carried out by Gamry electrochemical station at 1.45, 1.5 and 1.6 V by applying an alternated signal of 10 mV over the frequency range from 10k Hz to 0.1 Hz. Single cell durability is carried out on steady current density of 0.5 A cm^{-2} at 80 °C for 500 h.

Calculation method

The present first principle DFT calculations are performed by Vienna Ab initio Simulation Package(VASP)[4] with the projector augmented wave (PAW) method[5] . The exchange-functional is treated using the generalized gradient approximation (GGA) of Perdew-Burke-Ernzerhof (PBE)[6] functional. The Spin-polarizations were carried out for all calculations. The energy cutoff for the plane wave basis expansion was set to 450 eV and the force on each atom less than 0.05 eV/Å was set for convergence criterion of geometry relaxation. The Brillouin-zone integration was sampled by 2x2x1 point. The self-consistent calculations apply a convergence energy threshold of 10^{-5} eV. The DFT-D3 method was employed to consider the van der Waals interaction[7]. A 15 Å vacuum was added along the z direction in order to avoid the interaction between periodic structures.

The free energies of the OER were calculated by the equation:[8] $\Delta G = \Delta E_{DFT} + \Delta E_{ZPE} - T\Delta S$, where ΔE_{DFT} is the DFT electronic energy difference of each step, ΔE_{ZPE} and Δ_S are the correction of zero-point energy and the variation of entropy, respectively, which are obtained by vibration analysis, T is the temperature (T = 300 K).

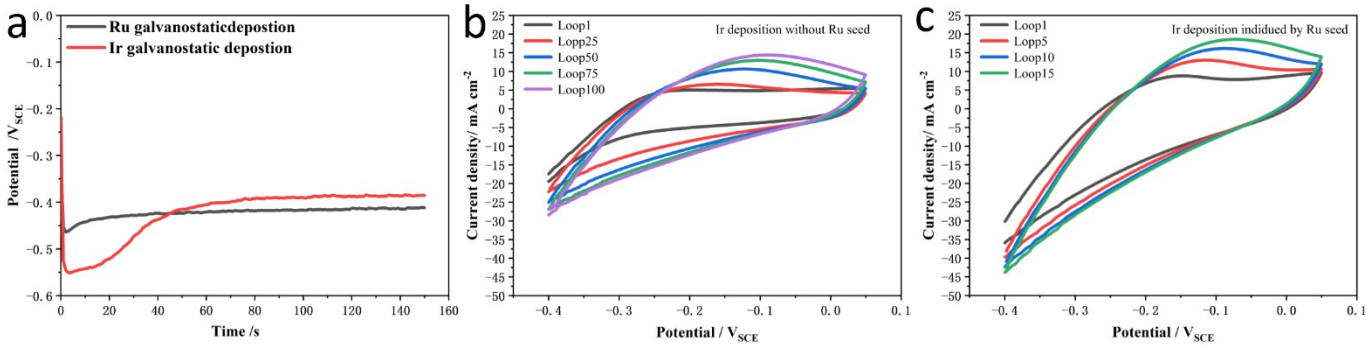

Fig. S1. Comparison of electrodeposition processes whether assisted by Ru seed. (a) First step conducted by Galvanostatic at a reduction current of 10 mA cm^{-2} in 80 °C $RuCl_3$ or H_2IrCl_6 depositing resolution. (b) Second step conducted by Cyclic voltammetry to prepared Ir coating without Ru seed assistant at 80°C H_2IrCl_6 depositing resolution. (c) Effective second step conducted by cyclic voltammetry to prepared Ir coating with Ru seed assistant at 80 °C H_2IrCl_6 depositing resolution.

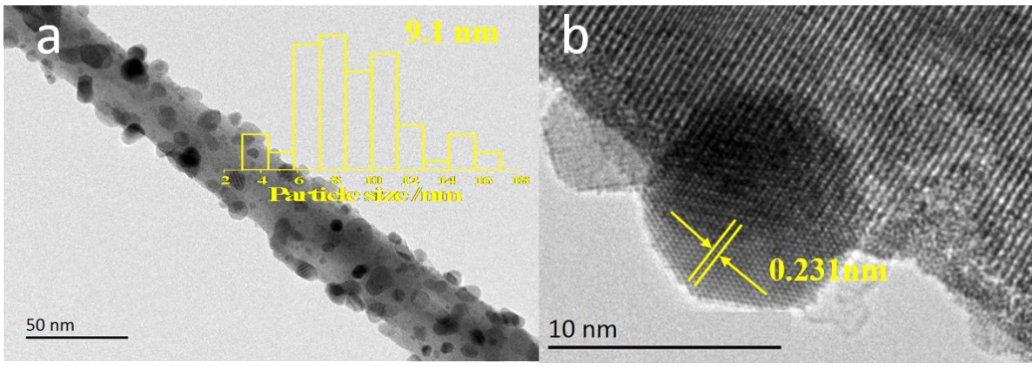

Fig. S2. Intermediate Ru@WO_3 TEM images. (a) Overall morphology of the nanorod with Ru seed size. **(b)** Locality morphology on Ru seed marked with interplanar spacing.

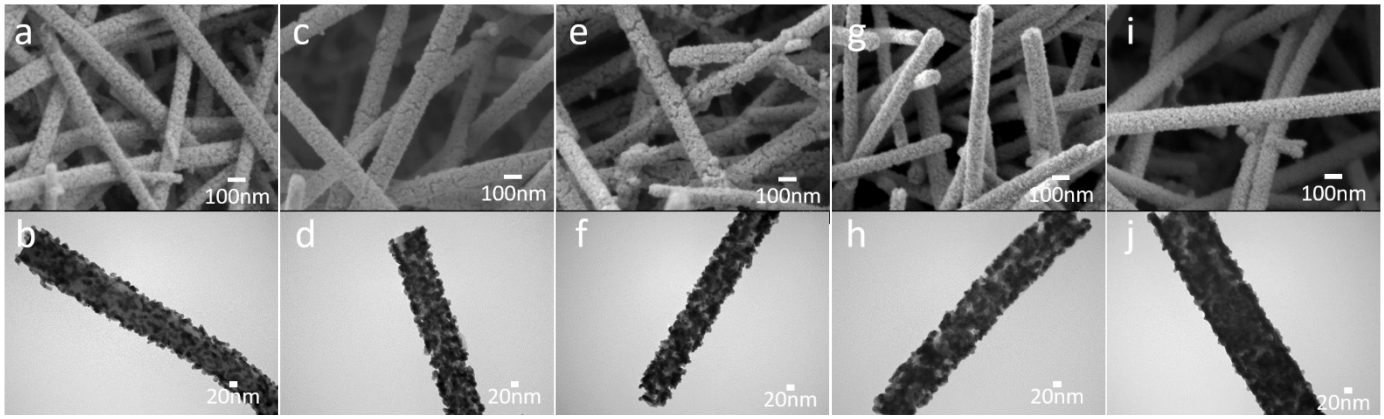

Fig. S3. Surface Ir/Ru ratio depended morphologies of (a-b) $Ir_{1.7}Ru_{0.9}@WO_3$, (c-d) $Ir_{3.5}Ru_1@WO_3$, (e-f) $Ir_{4.5}Ru_1@WO_3$, (g-h) $Ir_{3.2}Ru_{1.6}@WO_3$, (i-j) $Ir_{3.2}Ru_{1.6}@WO_3$.

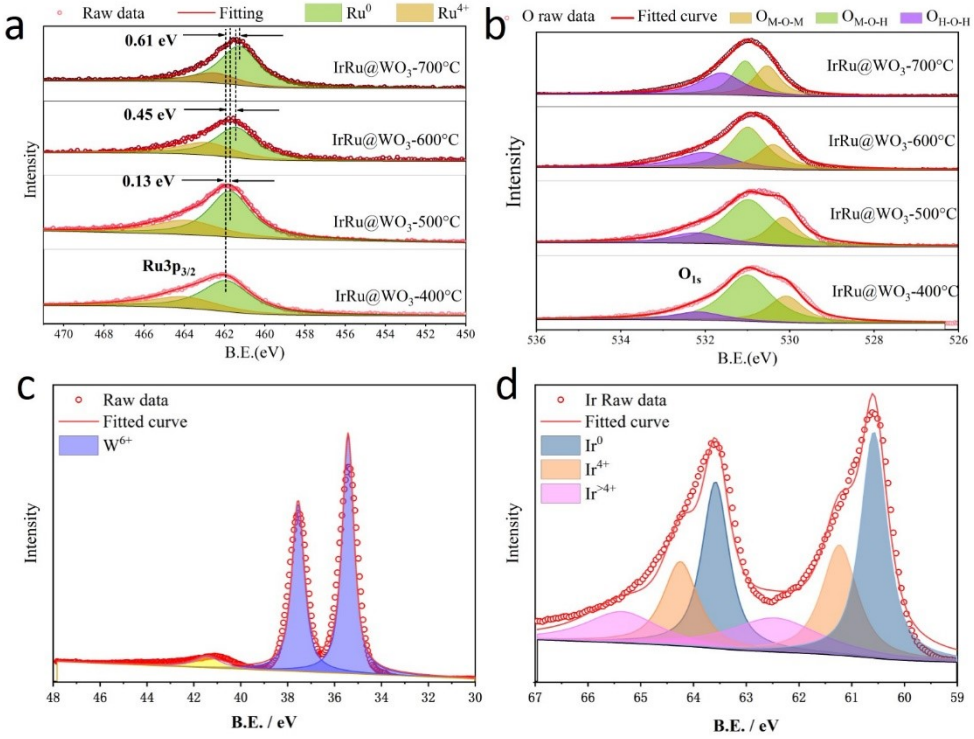

Fig. S4. Supplemental XPS result of IrRu@WO_3-400-700°C (a) Ru*3p* (b) O*1s*, (c) W*4f* of pure WO_3 and (d) Ir*4f* of commercial Ir Black(JM) spectrogram.

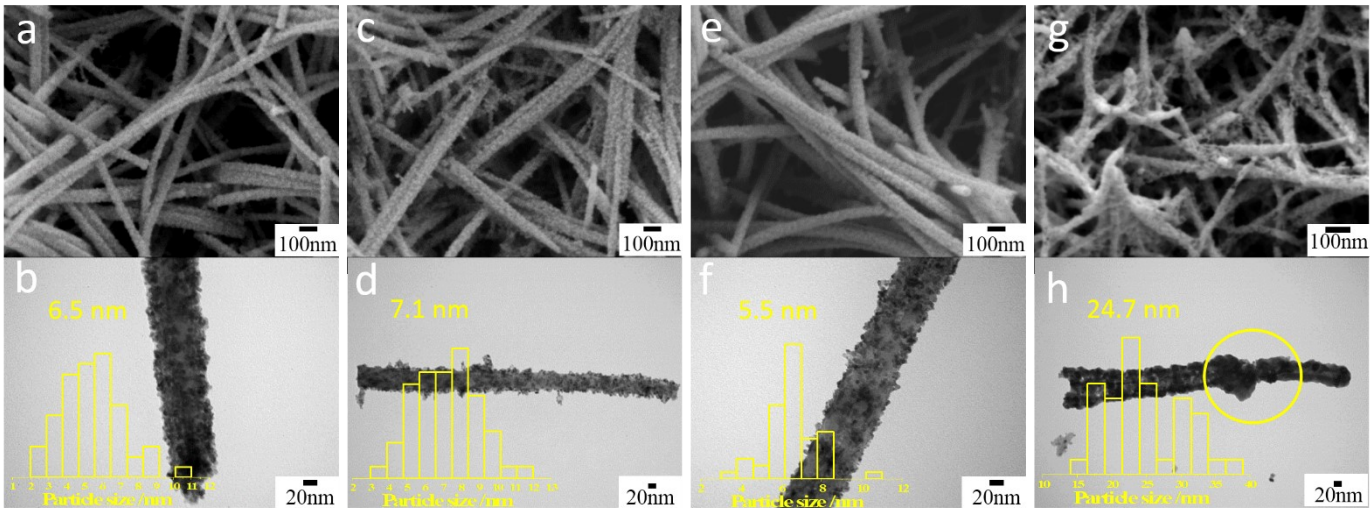

Fig. S5. Temperature depended morphologies of $Ir_{3.5}Ru_1@WO_3$ annealed in (a-b) 400 °C, (c-d) 500 °C, (e-f) 600 °C, (g-h) 700 °C.

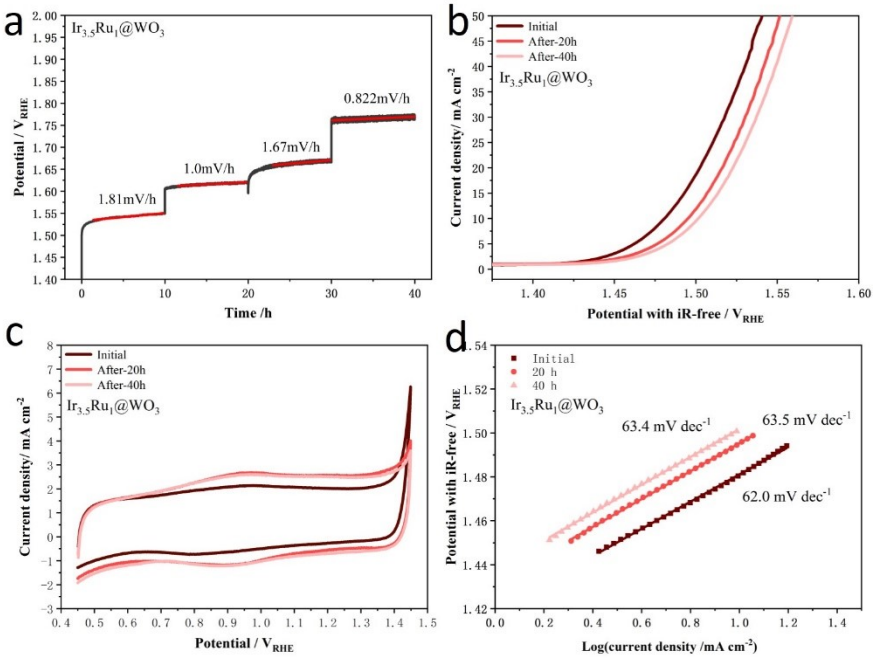

Fig. S6. The performance of $Ir_{3.5}Ru_1@WO_3$ during the stability operation tested in 0.5 M N_2-saturated H_2SO_4 at 30 °C. (a) Step chronopotentiometry operation at 10, 30, 50, 100 mA cm^{-2} for each step. (b) LSV curves, (c) CV curves, (d) Tafel curves at initial, after 20 h and 40 h operation.

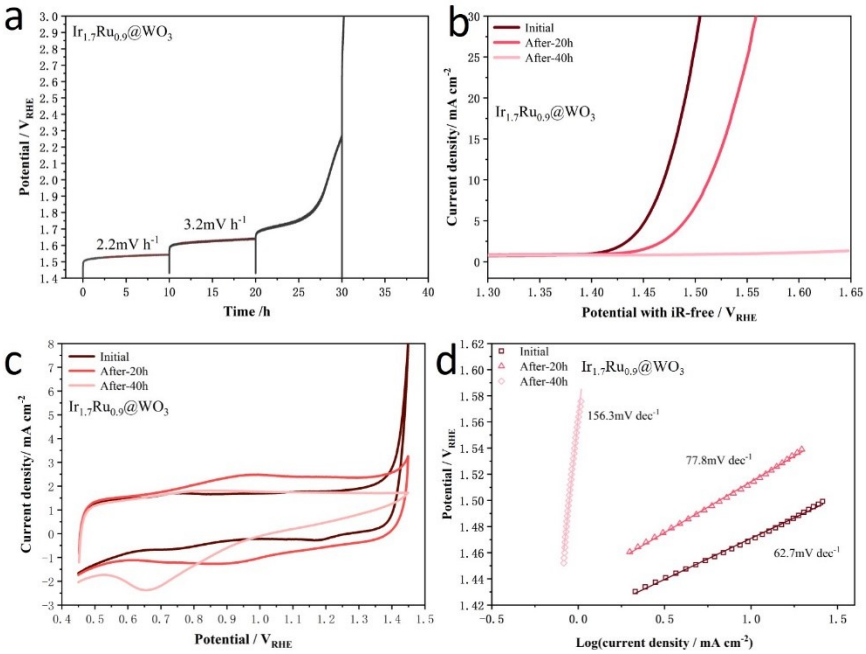

Fig. S7. Performance of $Ir_{1.7}Ru_{0.9}@WO_3$ during the stability operation tested in 0.5 M N_2-saturated H_2SO_4 at 30 °C. (a) Step chronopotentiometry operation at 10, 30, 50, 100 mA cm^{-2} for each step. (b) LSV curves, (c) CV curves, (d) Tafel curves at initial, after 10 h, 20 h, 30 h and 40 h operation.

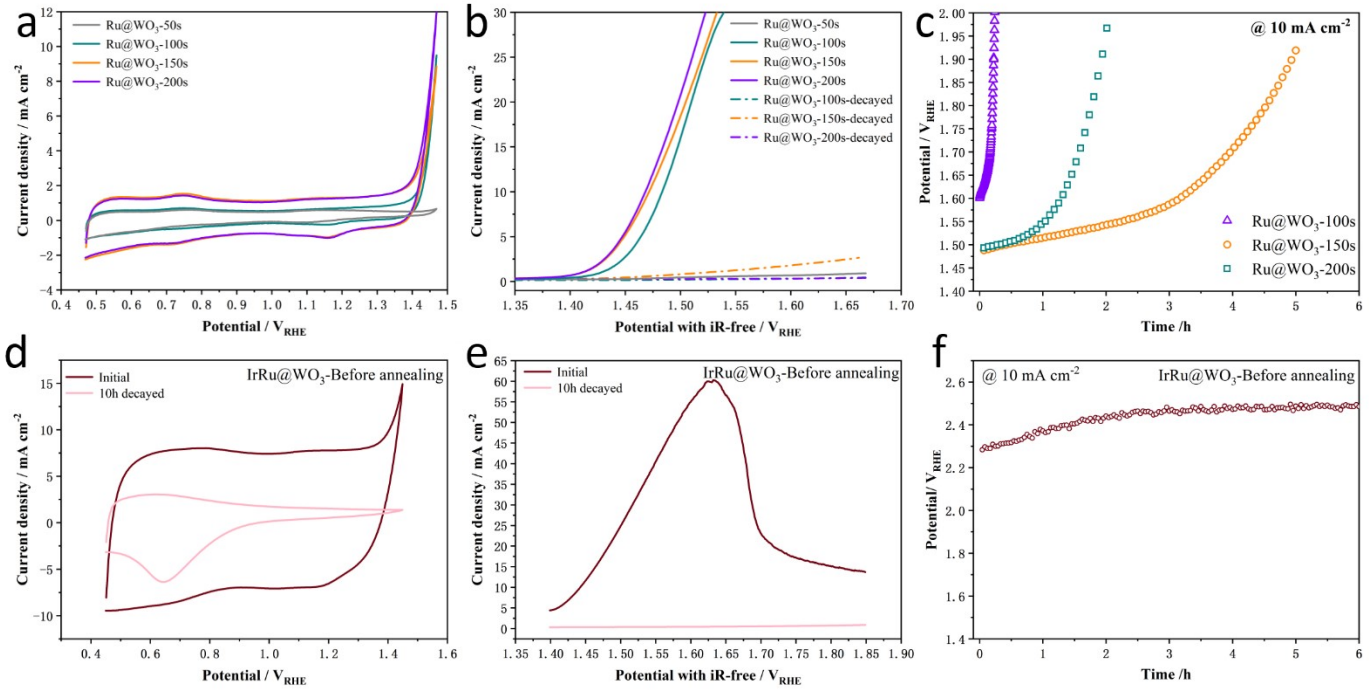

Fig. S8. OER performances for (a) CV curves, (b) LSV curves, (c) stability curves at 10 mA cm^{-2} of $Ru@WO_3$-600 °C with different deposition time; (d) CV curves, (e) LSV curves, (f) stability curves at 10 mA cm^{-2} of $IrRu@WO_3$ without annealing in 30 °C, 0.5 M N_2-saturated H_2SO_4.

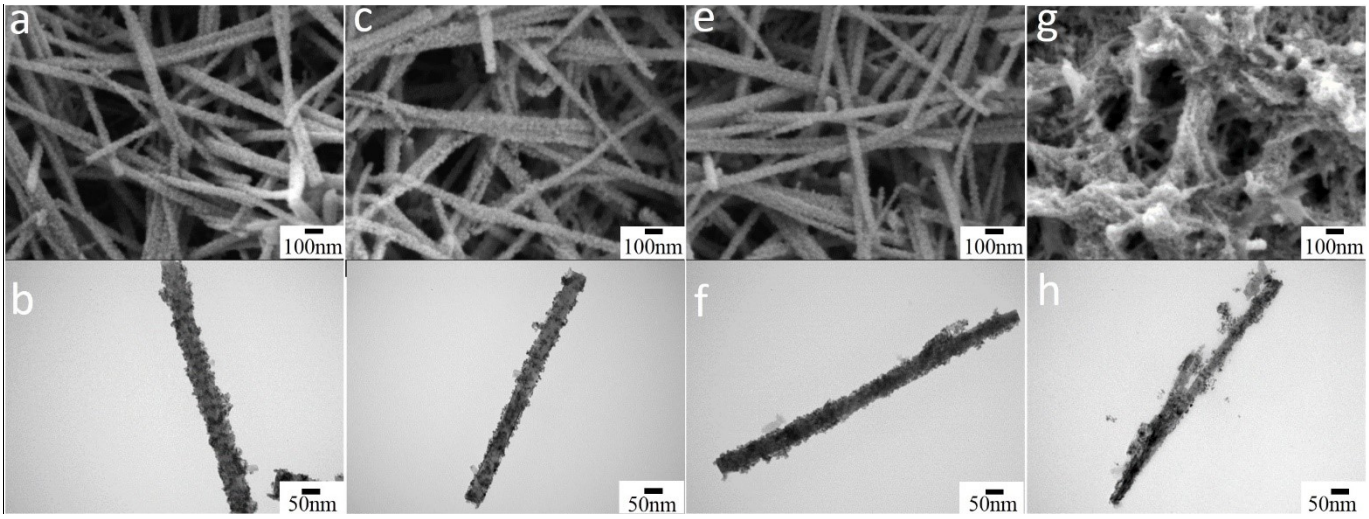

Fig. S9. Decayed morphologies of IrR@WO_3 annealed in (a-b) 400 °C, (c-d) 500 °C, (e-f) 600 °C, (g-h) 700 °C after operation.

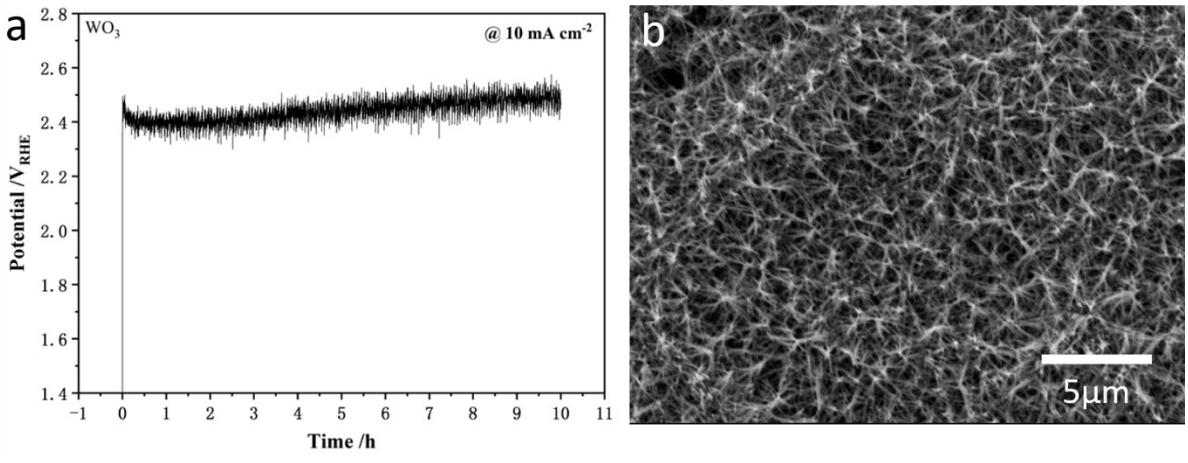

Fig. S10. Stability of pure WO_3. (a) Test of at 10 mA cm^{-2}, (b) the decayed morphology in SEM image.

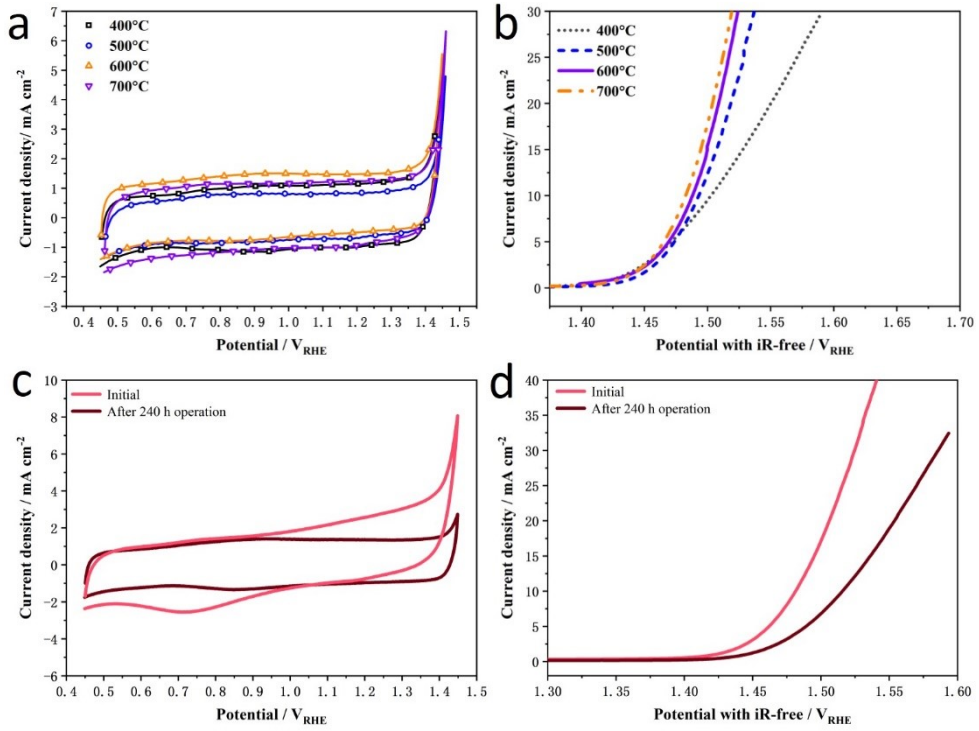

Fig. S11. OER performances of IrRu@WO_3 accompanying with annealing temperature 400~700°C, (a) CV and (b) LSV. (c)

CV and (d) LSV curve of IrRu@WO_3-600 before and after the 240 h stability test.

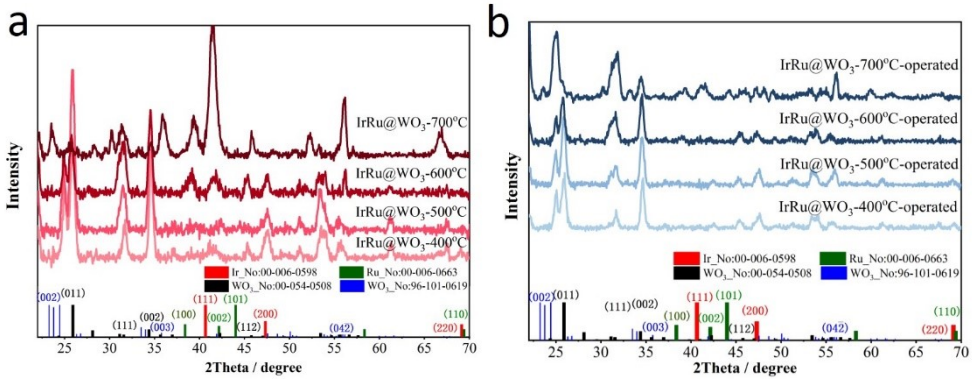

Fig. S12. XRD result of IrRu@WO_3 annealed in 400~700°C before (a) after (b) the step chronopotentiometry operation.

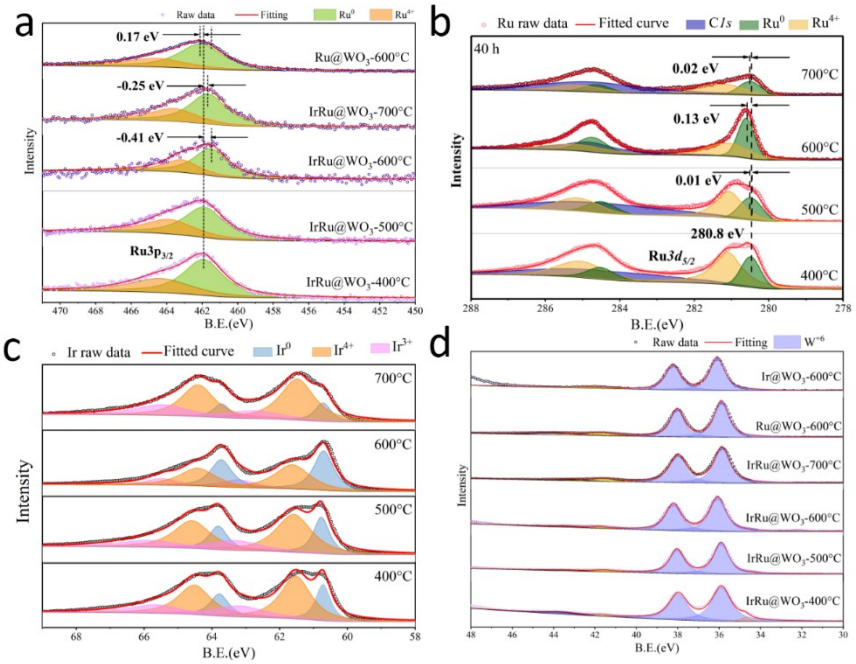

Fig. S13. Supplemental XPS of (a) Ru*3p*, (b) Ru*3d*, (c) Ir*4f* and (d) W*4f* of IrRu@WO_3 after the step chronopotentiometry operation.

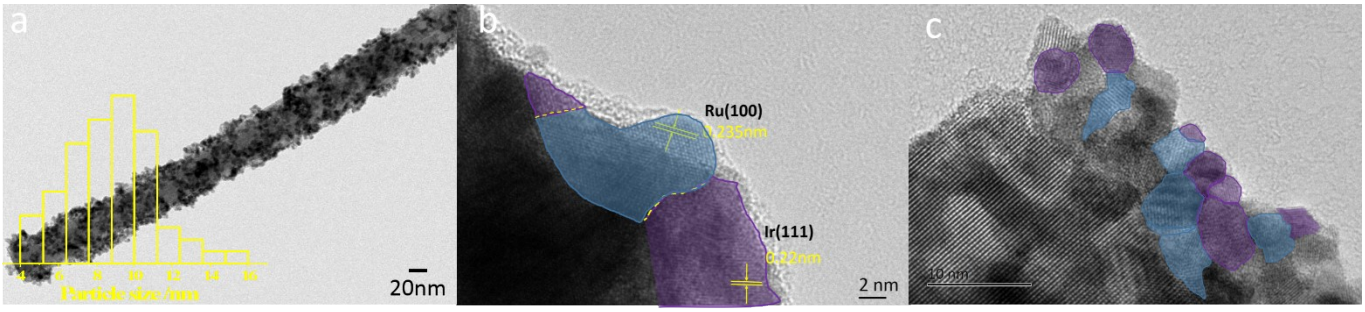

Fig. S14. TEM morphologies of IrRu@WO_3 after the stability operation. (a) Overall morphology of the nanorod with coating particle size. (b~c) Locality morphology with distinguished lattice figure marked by colored in blue (Ru) and purple (Ir).

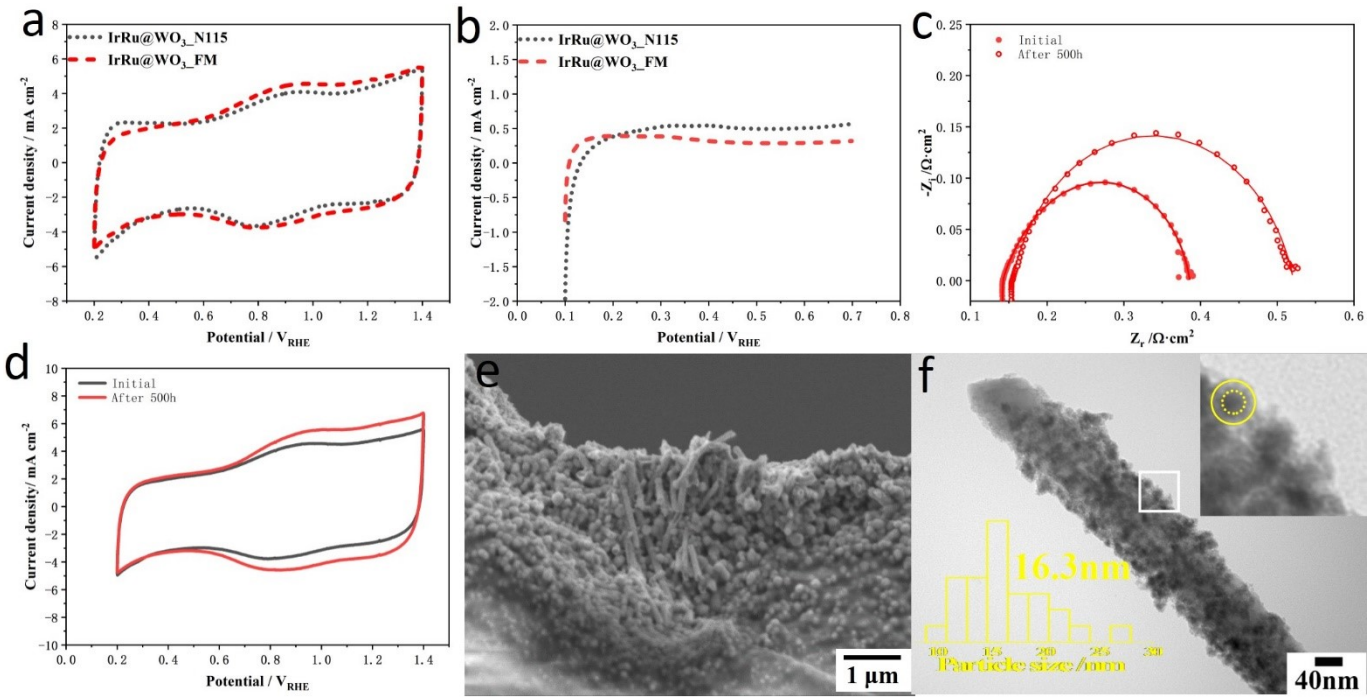

Fig. S15. The performance of IrRu@WO_3_N115 before and after 500 h lifetime. (a) Initial CV cure referenced to H_2 statured cathode at 30 °C, (b) Initial hydrogen permeation current at 30 °C, (c) EIS curve at 1.5 V, (d) CV curves lifetime referenced to H_2 statured cathode at 30 °C, (e) cross section SEM image of anode layer and (f) TEM image of anode catalyst.

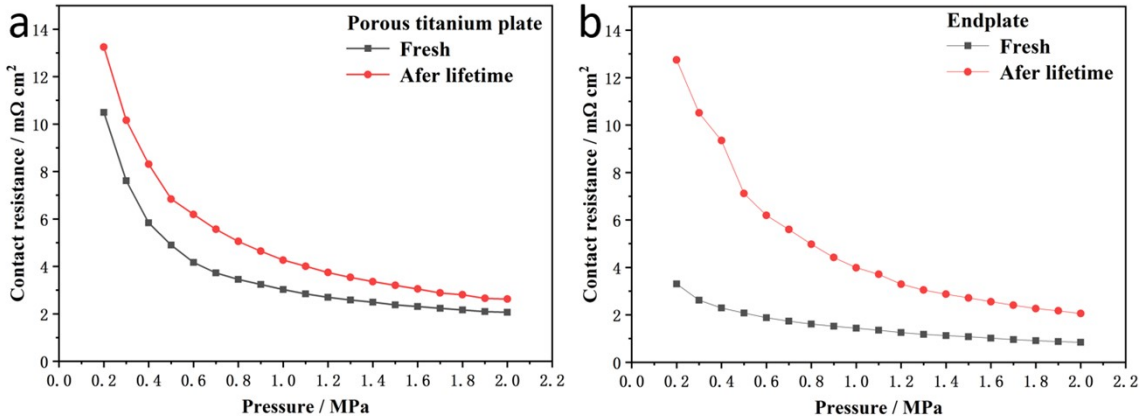

Fig. S16 Contact resistance of (a) porous titanium plate and (b) endplate before and after the 500h lifetime.

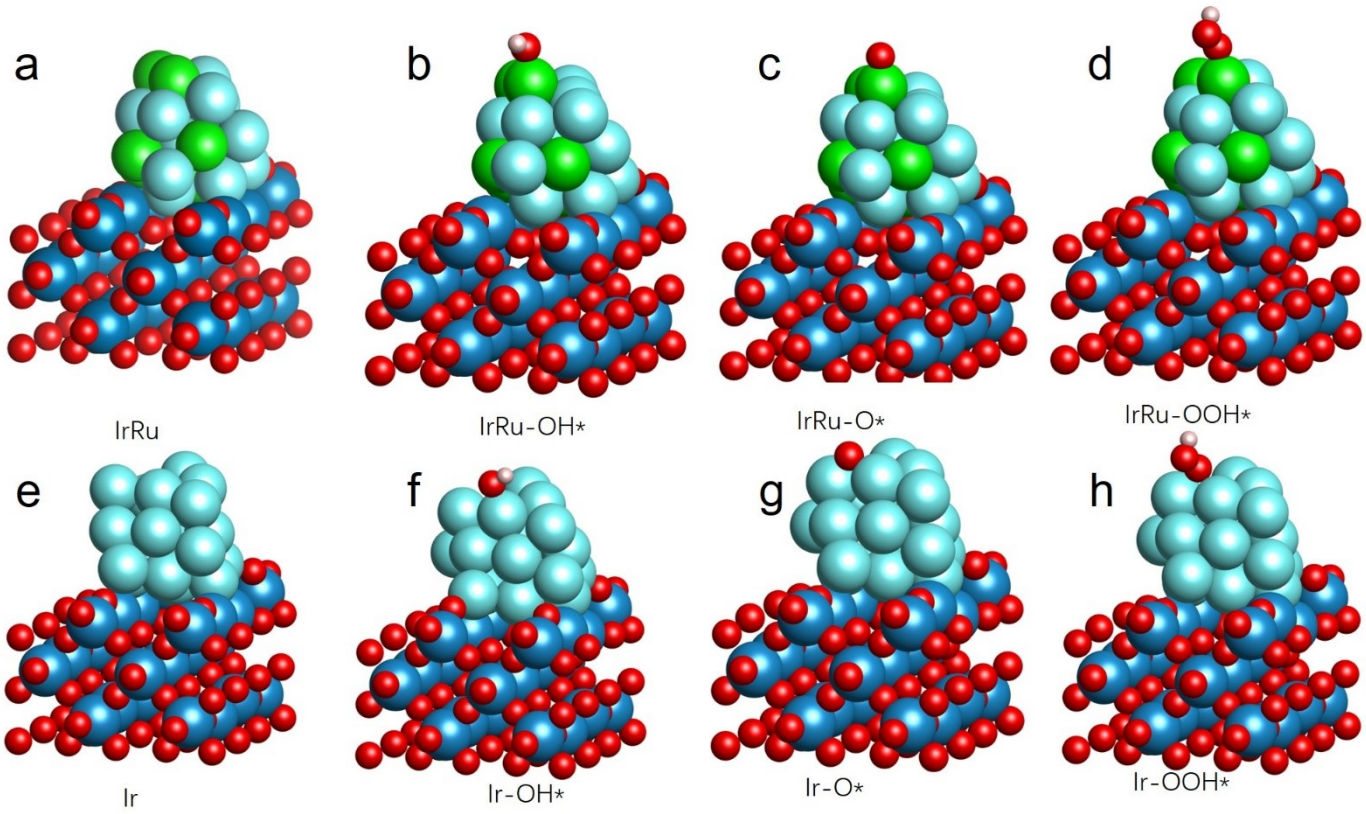

Fig. S17 Four-electron OER mechanism diagram for IrRu@WO_3(a-b) and Ir@WO_3(e-f) toward.

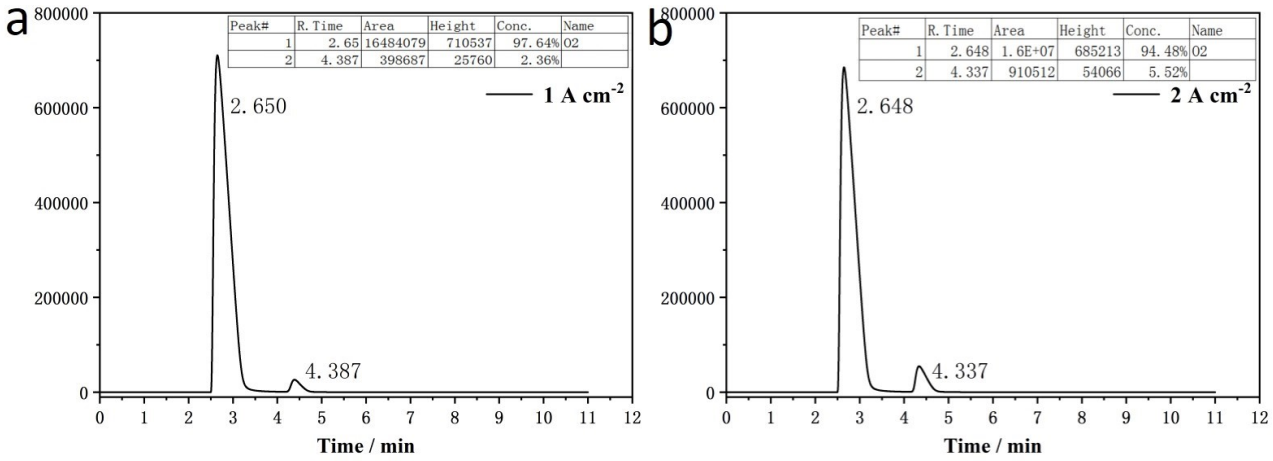

Fig. S18 Online GC result of the O_2 concentration in the anode gas at (a) 1.0 A cm^{-2} and (b) 2.0 A cm^{-2}.

Table 1. The detail depositing condition of the five samples in this work.

Experiment series	1#	2#	3#	4#	5#
Time of galvanostatic electrodeposition in $RuCl_3$ (aq) /s	100	100	100	150	200
Loop number of CV electrodeposition in H_2IrCl_6(aq)	5	10	15	10	10
Ir loading / μg cm^{-2}	57.7	114.9	151.9	105.5	102.5
Ru loading / μg cm^{-2}	16.4	17.8	17.2	28.0	57.5
Sample name	$Ir_{1.7}Ru_{0.9}@WO_3$	$Ir_{3.5}Ru_1@WO_3$	$Ir_{4.5}Ru_1@WO_3$	$Ir_{3.2}Ru_{1.6}@WO_3$	$Ir_{3.1}Ru_{3.2}@WO_3$

Table S2. Surface atomic ratio of Ir, Ru, W, O based on XPS.

Element	$Ir_{1.7}Ru_{0.9}@WO_3$	$Ir_{3.5}Ru_1@WO_3$	$Ir_{4.5}Ru_1@WO_3$
Ir	11.27	14.9	13.25
Ru	5.62	3.73	2.83
Surface Ir/Ru Ratio	2.0	3.99	4.68

Table S3. Quantitative XPS result from Ru*3d5/2* peak.

Ru*3d5/2*	Ru^0 /ev	Ru^{4+} /ev	Ir^0 position shifting /ev	Ru^0 area ratio /%	Ru^{4+} area ratio /%
IrRu@WO_3-400 °C	280.8	281.78	-	65.6	34.4
IrRu@WO_3-500 °C	280.57	281.21	-0.23	54.2	45.8
IrRu@WO_3-600 °C	280.55	281.0384	-0.25	40.7	59.3
IrRu@WO_3-700 °C	280.6	280.99	-0.2	57.8	42.2
IrRu@WO_3-400 °C -decayed	280.48	281.1	-0.68	30.4	69.6
IrRu@WO_3-500 °C -decayed	280.49	281.07	-0.14	34.1	65.9
IrRu@WO_3-600 °C -decayed	280.61	281.1	0.06	53.5	46.5
IrRu@WO_3-700 °C -decayed	280.5	281.25	0.26	39.7	60.3

Table S4. Quantitative XPS result from Ru*3p5/2* peak.

Ru*3p5/2*	Ru^0 /ev	Ru^{4+}/ev	Ru^0 position shifting /ev	Ru^0 area ratio /%	Ru^{4+} area ratio /%
IrRu@WO_3-400 °C	461.94	464.06	-	66.7	33.3
IrRu@WO_3-500 °C	461.69	463.87	-0.25	66.7	33.3
IrRu@WO_3-600 °C	461.48	463.08	-0.46	69.3	30.7
IrRu@WO_3-700 °C	462.41	464.82	0.47	67.2	32.8
IrRu@WO_3-400 °C-decayed	461.89	464.27	-0.05	61.7	38.3
IrRu@WO_3-500 °C-decayed	462.26	464.24	0.57	62.1	37.9
IrRu@WO_3-600 °C-decayed	461.89	463.55	0.41	67.8	32.2
IrRu@WO_3-700 °C-decayed	461.73	463.65	-0.68	64.8	35.2

Table S5. Quantitative XPS result from Ir*4f7/2* peak.

Ir*4f7/2*	Ir^0 /ev	Ir^{4+} /ev	$Ir^{>4+}$ /ev	Ir^0 position shifting /ev	Ir^0 area ratio /%	Ir^{4+} area ratio /%	$Ir^{>4+}$ area ratio /%
IrRu@WO_3-400°C	61.05	61.55	62.68	-	56.3	29.4	14.4
IrRu@WO_3-500 °C	61.12	61.82	63.21	0.07	44.9	40.4	14.8

IrRu@WO_3-600 °C	61.21	61.55	62.81	0.16458	48.0	31.5	20.5
IrRu@WO_3-700 °C	61.29	61.96	63.08	0.24	77.8	14.8	7.4
IrRu@WO_3-400 °C -decayed	61.21	62.05	62.96	0.16	31.7	28.3	40.0
IrRu@WO_3-500 °C -decayed	61.06	61.86	62.7	-0.06	23.2	41.1	35.7
IrRu@WO_3-600 °C -decayed	61.28	62.09	63.03	0.07	34.9	26.1	39.0
IrRu@WO_3-700 °C -decayed	61.05	61.83	63.24	-0.24	10.3	59.7	30.0

Table S6. OER performance summary in congeneric references

Reference number	Catalyst	Overpotential	Single cell performance	
		mV@10 mA cm^{-2}	Ir loading (mg cm^{-2})	*I*@*V*_ Electrolyte membrane
[9]	IrO_2	313	4.0	2.0 A cm^{-2}@2.15V@N117
[1]	Ir@WO_3	310	0.144	3.0 A cm^{-2}@2.19V@N115
[10]	La_3IrO_7	296	--	--
[11]	IrO_2@Ir/TiN	265	--	--
[12]	PtIr	--	0.15	4.0 A cm^{-2}@2.25V@N115
[13]	$Ir_{0.7}Ru_{0.3}O_x$	--	0.28	3 A cm^{-2}@1.85_Aquivion®SSC
[14]	IrO_2	--	0.02	2.1 A cm^{-2}@2.0V_N212
[15]	IrO_2@TiO_2	450	0.4	5.0 A cm^{-2}@2.07V_N212
[16]	Ir@TiO_2-MoO_x	290	0.5	1.95 A cm^{-2}@1.95V_N115
[17]	Ir-W	290	1	1.0 A cm^{-2}@1.75V_N117
[18]	$Ir_{0.7}Ru_{0.3}O_x$	275	0.82	1.0 A cm^{-2}@1.7V_N212

Notes and references

1. G. Jiang, H. M. Yu, Y. H. Li, D. W. Yao, J. Chi, S. C. Sun and Z. G. Shao, *Acs Applied Materials & Interfaces*, 2021, **13**, 15073-15082.
2. K. K. Zhang, W. S. Mai, J. Li, H. Wang, G. Q. Li and W. Hu, *J. Mater. Sci.*, 2020, **55**, 3507-3520.
3. G. Jiang, H. M. Yu, J. K. Hao, J. Chi, Z. X. Fan, D. W. Yao, B. W. Qin and Z. G. Shao, *J. Energy Chem.*, 2019, **39**, 23-28.
4. P. E. Blochl, *Physical Review B*, 1994, **50**, 17953-17979.
5. G. Kresse and J. Furthmuller, *Computational Materials Science*, 1996, **6**, 15-50.
6. K. A. Maerzke, G. Murdachaew, C. J. Mundy, G. K. Schenter and J. I. Siepmann, *J. Phys. Chem. A*, 2009, **113**, 2075-2085.
7. J. P. Perdew, J. A. Chevary, S. H. Vosko, K. A. Jackson, M. R. Pederson, D. J. Singh and C. Fiolhais, *Physical Review B*, 1992, **46**, 6671-6687.
8. E. Skulason, T. Bligaard, S. Gudmundsdottir, F. Studt, J. Rossmeisl, F. Abild-Pedersen, T. Vegge, H. Jonsson and J. K. Norskov, *Physical Chemistry Chemical Physics*, 2012, **14**, 1235-1245.
9. Z. P. Yu, J. Y. Xu, Y. F. Li, B. Wei, N. Zhang, Y. Li, O. Bondarchuk, H. W. Miao, A. Araujo, Z. C. Wang, J. L. Faria, Y. Y. Liu and L. F. Liu, *Journal of Materials Chemistry A*, 2020, **8**, 24743-24751.
10. Q. Qin, H. Jang, Y. M. Wang, L. J. Zhang, Z. J. Li, M. G. Kim, S. G. Liu, X. E. Liu and J. Cho, *Adv. Energy Mater.*, 2021, **11**, 8.
11. G. Li, K. Li, L. Yang, J. Chang, R. Ma, Z. Wu, J. Ge, C. Liu and W. Xing, *ACS Applied Materials & Interfaces*, 2018, 38117-38124.
12. M. K. Debe, S. M. Hendricks, G. D. Vernstrom, M. Meyers, M. Brostrom, M. Stephens, Q. Chan, J. Willey, M. Hamden, C.

K. Mittelsteadt, C. B. Capuano, K. E. Ayers and E. B. Anderson, *J. Electrochem. Soc.*, 2012, **159**, 165-176.

13. S. Siracusano, N. Hodnik, P. Jovanovic, F. Ruiz-Zepeda, M. Šala, V. Baglio and A. S. Aricò, *Nano Energy* 2017, **40** 618–632.
14. J. E. Park, S. Kim, O. H. Kim, C. Y. Ahn, M. J. Kim, S. Y. Kang, T. I. Jeon, J. G. Shim, D. W. Lee, J. H. Lee, Y. H. Cho and Y. E. Sung, *Nano Energy*, 2019, **58**, 158-166.
15. C. Van Pham, M. Buhler, J. Knoppel, M. Bierling, D. Seeberger, D. Escalera-Lopez, K. J. J. Mayrhofer, S. Cherevko and S. Thiele, *Appl. Catal. B-Environ.*, 2020, **269**, 1-12.
16. E. J. Kim, J. Shin, J. Bak, S. J. Lee, K. H. Kim, D. Song, J. Roh, Y. Lee, H. Kim, K. S. Lee and E. Cho, *Appl. Catal. B-Environ.*, 2021, **280**, 9.
17. J. J. Gao, X. Huang, W. Z. Cai, Q. L. Wang, C. M. Jia and B. Liu, *Acs Applied Materials & Interfaces*, 2020, **12**, 25991-26001.
18. L. Wang, V. A. Saveleva, S. Zafeiratos, E. R. Savinova, P. Lettenmeier, P. Gazdzicki, A. S. Gago and K. A. Friedrich, *Nano Energy*, 2017, **34**, 385-391.